Supplementary Materials for

Asymmetric interactions and feast–famine cycles drive chaos in microbial populations

William F. McLaughlin[†], Thomas Beardsley[†], Natalia L. Komarova[*], & Megan G. Behringer[*]

[†]These authors contributed equally to this work.

[*]Corresponding author. Email: nkomarova@ucsd.edu, megan.g.behringer@vanderbilt.edu

This PDF file includes:

Supplementary Text
Figures S1 to S16
Tables S1 to S2
Caption for Movie S1
Supplementary References

Supplementary Text

Introductory Material

Dynamic models of microbial growth primarily fall into two categories: (1) those that model interaction characteristics directly, as in Lotka-Volterra type equations, and (2) those that mediate interactions and fitness through resources in what we call Consumer-Resource (CR) equations. The generalized Lotka-Volterra (gLV) equations, which describe the concentration of n taxons through their pairwise interactions, are formulated as

$$\frac{\mathrm{d}X_i}{\mathrm{d}t} = X_i\left(r_i + \sum_{j=1}^{n} a_{ij}X_j\right) \text{ for } i = 1, 2, \ldots, n. \tag{S1}$$

The only dynamics described in gLV models are those for the concentrations of the taxons themselves (values X_i), and they depend only on their base fitness values, r_i, and the interaction coefficients a_{ij}. Consumer-Resource models distinguishes between the taxons, X_i, and resources R_i. In CR models, interactions are mediated by resource concentration as opposed to the pairwise terms that appear in gLV models. For example, n communities competing over a single resource in a batch culture would be described by

$$\begin{aligned}\frac{\mathrm{d}X_i}{\mathrm{d}t} &= f_i(R)X_i - d_iX_i \text{ for } i = 1, 2, \ldots, n,\\ \frac{\mathrm{d}R}{\mathrm{d}t} &= -\sum_{i=1}^{n} f_i(R)\frac{X_i}{y_i},\end{aligned} \tag{S2}$$

where d_i is the death rate of X_i, y_i is the yield coefficient and f_i is the response function. The Holling type 2 response function (*1*) is a reparameterization of the Monod growth curve (*2*) which we employ below. Monod growth describes the growth of a microorganism as a function of the concentration of a substrate such that in the context of equation (S2),

$$f_i(R) = b_i\frac{R}{k_i + R}, \tag{S3}$$

where b_i is the maximal exponential growth rate, R is the concentration of the resource, and k_i is the half-velocity constant, defined such that $f_i(k_i) = 1/2$. A model of a single community's concentration with respect to a single resource is given by

$$\begin{aligned}\frac{\mathrm{d}X}{\mathrm{d}t} &= X\left(b\frac{R}{k + R} - d\right),\\ \frac{\mathrm{d}R}{\mathrm{d}t} &= -\beta X\frac{R}{k + R}.\end{aligned} \tag{S4}$$

By including additional resources and consumers to equation (S4), we can model common ecological interactions. Keeping only one resource and adding consumers can model competition for a single resource, or perhaps adding more resources and changing the sign of their β coefficients can determine if they are producers or consumers of that resource. We are interested in the *auxotroph over-producer* relationship. When we consider a single strain of a bacterium identifiable subclades may form from different mutations. A subclade that requires a resource that the original strain did

not is called an auxotroph and a subclade that produces more of a resource than the orginal is called an over-producer.

To model the auxotroph over-producer relationship we add a resource corresponding to the nutrient produced by the over-producer and required by the auxotroph.

Definition 1. (Noncompetitive Crossfeeder Model) In equation (S5) below, the concentrations X_1 and X_2 refer to the over-producer and auxotroph respectively. Resource R_1 is the limiting resource for the over-producer X_1 and R_2 is the metabolite required by the auxotroph X_2. The coefficients b_{ii} are the maximal growth coefficients, k_{ii} are the half-velocity constants, and d_i are death rates. The coefficients $\beta_{ij} = b_{ij}/y_{ij}$ are reparameterizations of the yield coefficients:

$$\begin{aligned}
\frac{\mathrm{d}X_1}{\mathrm{d}t} &= X_1\left(b_{11}\frac{R_1}{k_{11}+R_1} - d_1\right)\\
\frac{\mathrm{d}X_2}{\mathrm{d}t} &= X_2\left(b_{22}\frac{R_2}{k_{22}+R_2} - d_2\right)\\
\frac{\mathrm{d}R_1}{\mathrm{d}t} &= -\beta_{11}X_1\frac{R_1}{k_{11}+R_1}\\
\frac{\mathrm{d}R_2}{\mathrm{d}t} &= \beta_{12}X_1\frac{R_1}{k_{11}+R_1} - \beta_{22}X_2\frac{R_2}{k_{22}+R_2}
\end{aligned} \tag{S5}$$

This simplified model decouples resource usage and does not explicitly include terms for lag or stationary phases. The separate resource usage suggests R_i is the limiting resource for X_i for $i = 1, 2$. Model (S5) can be thought of as a sub-model of more complex models, for example if there were competition for R_1, but the over-producer auxotroph relationship is maintained for R_2 as in equation (S6).

Definition 2. (Competitive Crossfeeder Model) The coefficients in equation (S6) are defined in the same way as equation (S5) where b_{ij} and k_{ij} are the maximum growth and half-velocity constants of X_i with respect to R_j:

$$\begin{aligned}
\frac{\mathrm{d}X_1}{\mathrm{d}t} &= X_1\left(b_{11}\frac{R_1}{k_{11}+R_1} - d_1\right)\\
\frac{\mathrm{d}X_2}{\mathrm{d}t} &= X_2\left(b_{21}\frac{R_1}{k_{21}+R_1} + b_{22}\frac{R_2}{k_{22}+R_2} - d_2\right)\\
\frac{\mathrm{d}R_1}{\mathrm{d}t} &= -\beta_{11}X_1\frac{R_1}{k_{11}+R_1} - \beta_{21}X_2\frac{R_1}{k_{21}+R_1}\\
\frac{\mathrm{d}R_2}{\mathrm{d}t} &= \beta_{12}X_1\frac{R_1}{k_{11}+R_1} - \beta_{22}X_2\frac{R_2}{k_{22}+R_2}.
\end{aligned} \tag{S6}$$

Note that model (S4) is a submodel of (S5) and (S5) is a submodel of (S6) in the sense that if $b_{21} = \beta_{21} = 0$, then equations (S6) are identical to (S5). Similarly, eliminating the dimensions and coefficients for X_2 and R_2 in equation (S5), yields equation (S4).

We seek to model the process of serial transfer cultures through a process where an underlying system propagates through an interval (t_n, t_{n+1}) and at time t_{n+1} a 'transfer' is made instantaneously by introducing a discontinuous impulse in the flow of the underlying system that dilutes the existing culture and replaces consumed nutrients. Examples of experimental data obtained by serial dilution are given in figure **S4**.

Definition 3. (Serial Transfer Model) Let $\dot{Y} = f(Y)$ denote either model (S5) or (S6) where $Y_i = X_i$ and $Y_j = R_{j-2}$ for $i = 1, 2$ and $j = 3, 4$. Let $\tau > 0$ be the transfer interval such that the transfer times are $n\tau$ for $n = 1, 2, 3, \ldots$ and let $\phi : \mathbb{R}^n \to \mathbb{R}^n$ be the instantaneous transfer function. Define $U : \mathbb{R} \times \mathbb{R}^4 \to \mathbb{R}^4$ to be the forward operator such that

$$U(t, Y_0) = Y(t)$$

where $Y(t)$ is the solution to the initial value problem $\dot{Y} = f(Y)$, $Y(0) = Y_0$. Then define serial transfer map

$$G_t(Y_0) = \phi \circ U(t, Y_0). \tag{S7}$$

Repeated applications of the map (S7) define a discontinuous set of semi-flows, Y, with the properties

$$\begin{cases} \dot{Y}(t) = f(Y) \text{ for } t \neq n\tau \\ Y(t+) = \phi(Y(t-)) \text{ for } t = n\tau \end{cases} \tag{S8}$$

For models (S5) and (S6) we define $\phi_1(x) = \phi_2(x) = \phi_4(x) = rx$ and $\phi_3(x) = (1-r)(Y_0)_3 + rx$ where r is the dilution fraction and $(Y_0)_3$ the third component of Y_0, which is the initial concentration of R_1. The component functions ϕ_1, ϕ_2, and ϕ_4, denote the transfer of the contents of one culture to the next; the component ϕ_3 denotes both the transfer of the contents of a previous culture, the rx term, and the concentration of the nutrient in the fresh medium, the $(1-r)(Y_0)_3$ term.

Definition 4. (Discrete Time Map) Let $U : \mathbb{R} \times \mathbb{R}^4 \to \mathbb{R}^4$ be the forward operator and ϕ be the transfer function defined in definition (3). Define $H_t : \mathbb{R}^4 \to \mathbb{R}^4$ by

$$H_t(x) = U(t, \phi(x)). \tag{S9}$$

Then the sequence

$$x_1 = U(\tau, x_0) \tag{S10}$$
$$x_n = H_\tau(x_{n-1}) \text{ for } n > 1 \tag{S11}$$

corresponds to the sequence of values $Y(t-)$ for $t = \tau n$ as defined in definition (3). The sequence $\{x_i\}_{i=0}^{\infty}$ we refer to as the discrete time map or just *discrete map*.

Model Characteristics

Note that there are no fixed points for model (S5) or (S6) where X_1 or X_2 are positive. Considering model (S5) if there is a fixed point with $X_i > 0$ then we must have $R_i/(k_{ii} + R_i) = d_i/b_{ii}$. For $i = 1$ this would imply $-\beta_{11} X_1 d_1/b_{11} = 0$ which is a contradiction. Similarly, for $i = 2$ we know $X_1 = 0$ (by the previous sentence) thus we would have $-\beta_{22} X_2 d_2/b_{22} = 0$, again a contradiction.

For system (S6) if we assume either $X_1 = 0$ or $X_2 = 0$ then similar reasoning to the previous paragraph will imply the other must be zero as well. If we assume both $X_1 > 0$ and $X_2 > 0$ then the equation $\frac{dR}{dt} = 0$ implies that $R_1/(k_{11} + R_1)$ and $R_1/(k_{21} + R_1)$ have opposite signs when $R_1 > 0$ which is a contradiction as $\beta_{ij}, k_{ij} > 0$ for all i, j and $R_1 > 0$ by assumption. Thus, all fixed points for both models (S5) and (S6) have the form $X_1 = X_2 = 0$ and $R_1, R_2 \in \mathbb{R}$.

Calibration Methodology

To calibrate specific examples we take advantage of the nested property of models (S4), (S5), and (S6). In order to scale coefficients, we first determine a 'general fit' to an underlying growth curve. This is done sequentially:

1. Calibrate a monoculture model, equation (S4), to the growth data of the overproducer.
2. Fix the parameters of the overproducer in (S4) as nested in model (S5), and calibrate the remaining parameters, $b_{22}, k_{22}, d_2, \beta_{12}$, and β_{22}, to the growth curve of the auxotroph.
3. Include all parameters of the calibrated model (S5) as fixed in model (S6), and fit the competitive parameters b_{21}, k_{21}, and β_{21}.
4. Finally, let p be the vector of parameters of model (S6). Choose a set of bounds $l, u \in \mathbb{R}^m$ such that $l_i \leq p_i \leq u_i$ and allow parameters to vary within the box $\{x \in \mathbb{R}^m : l_i \leq x \leq u_i\}$ for a final optimization pass conducted on all parameters of equation (S6).

These steps generate a system with the form of equations (S6) that is a best fit for the growth curve data over single time period, where no transfers as in definition (3) occurs. An example of data over a single time period is given in figure **S5**. The result is a best fit relative to the loss function and produces a local minimum, given the nonconvex nature of the optimization problems involved. This system shares some important properties with the underlying growth data. In particular, model (S6) produces an averaged growth and death phase that track the underlying dynamics, although more subtle stationary and lag phases are not directly captured.

Taking the set of parameters obtained from step (4.) and simulating a sequence of serial transfers as described in definition (3) commonly produces a sequence of trajectories that converge in the sense that the values $Y(t+)$ for $t = n\tau, n = 1, 2, \ldots$ converge as a vector in $\mathbb{R}^4$. This will, in the limit, produce a periodic trajectory for $Y(t)$ and constant sequence $Y(\tau n+)$, see figure **S7**. Note that, as there are discontinuities at time points $n\tau$, this convergence can in fact occur in finite time.

While large swathes of the parameter space produce convergent sequences of the values of $Y(n\tau+)$, there are open sets of parameter space which produce sequences of $Y(n\tau+)$ that are periodic, sometimes with very high period, or even aperiodic. To capture the seemingly chaotic behavior of the relative abundance data, see figure **S4**, we implement further fitting steps that involve serial passaging data:

5. Let p^* be the vector of calibrated parameters obtained in step (4.). Choose new upper and lower bounds $l', u' \in \mathbb{R}^m$ such that $l'_i \leq p^*_i \leq u'_i$ and define the box $P = \{x \in \mathbb{R}^m : l'_i \leq x_i \leq u'_i\}$, and sample uniformly from P.
6. Simulate each sample and find an example than reasonably minimizes the residual sum of squares of the relative values. That is, we want to minimize the differences

$$\sum_{i=1}^{2} \sum_{j=1}^{n} \left(\frac{X_i(t_j, p)}{X_1(t_j, p) + X_2(t_j, p)} - \frac{\hat{x}_i(t_j)}{\hat{x}_1(t_j) + \hat{x}_2(t_j)} \right)^2 \tag{S12}$$

with respect to $p \in P$, where $\hat{x}_i(t_j)$ are the measurements obtained from a serial transfer experiment.

7. Using the parameters obtained in step (6.) as initial values, do a final optimization round minimizing the loss function (S12) producing a calibrated parameter vector $\hat{p}$.

These steps generate a parameter set that is a best fit of the relative abundance values of the serial passage data, as in panel (A) of figure **S4**, while the details of the absolute growth values may differ from the initial reference values used in steps (1)-(4). It is important to note that the experimental conditions driving the dynamics in the 20-day culture, such as figure **S6**, are different from those in the longer-term, serial dilution experiments such as figure **S4**. The initial inoculation for 20-day growth experiments starts at an initial value of 0 for R_2, whereas under serial dilutions, a positive value of R_2 is present after each passaging. Therefore, parameter values that we estimate from steps (1-4) are not expected to be exactly the same as those in steps (5-7). Instead, they serve to establish reasonable ranges for the parameters that characterize the dynamics in the long-term serial dilution experiments.

The process of finding areas in the parameter space that display some non-periodic behavior is dependent on the initial calibration of parameters. Say, as a trivial example, we find all parameters are zero except for d_1, and our parameter box contains only a cylinder around d_1, then every solution will converge to zero, and there will be no nontrivial periodicity or aperiodicity of Y at the dilution times $n\tau$. If, however, a given set of parameters produces periodic solutions to equation (S7), then small changes to the parameters can have large effects on the trajectories. As a result, identifying a set where the trajectory, $Y(t)$, is sensitive to initial values is critical to fitting aperiodic relative growth values. To do this, we may split step (6.) into two separate steps

6a. Sample from P and search for parameter vectors p that display aperiodic behavior at points $n\tau$. These need not match any data.

6b. For each p identified in (6a.) construct a new box P'' with bounds $\{l_i'', u_i''\}$ such that $p \in \prod_i [l_i'', u_i'']$. Sample P'' to minimize quantity (S12), and continue as above.

This is a nondeterministic procedure. A grid search in the parameter space may be practical for very small sets, but quickly becomes computationally daunting for larger sets. As we are ultimately looking for solutions that match relative abundances of empirical measurements, a direct global optimization over the entire parameter space, $\mathbb{R}^{12}$ for equation (S6), is unreasonable. Additionally gradient based methods performed quite poorly. We used differential evolution based optimization algorithms for minimization, specifically the `BBO_adaptive_de_rand_1_bin` method of the `BlackBoxOptim.jl` package included with the `Optimization.jl` package (*3*). These methods perform a global gradient free optimization over a region in $\mathbb{R}^n$ defined by the product of intervals $[l_1, u_1] \times [l_2, u_2] \times \ldots \times [l_n, u_n]$. We use steps (1.-4.) to determine a reasonable set of bounds for steps (5.-7.). This is effective because the number of parameters over which which we optimize in steps (1.-4.) is much smaller. We start out in step 1 optimizing over just 4 parameters in the box $[0, 100]^4$ then sequentially fixing previous parameters and optimizing over new parameters to arrive at scales of the parameters that produce empirically feasible trajectories at step 4.

These parameters then serve as a starting point for steps (5.-7.). When we construct the bounds in step 5, we do so by first choosing factors $0 < a < 1$ and $1 < b$, and setting $l_i' = ap_i^*$ and $u_i' = \max\{bp_i^*, \mu\}$ for some $\mu > 0$ to avoid intervals that are too narrow when p_i^* is small. Steps (5-7) then result in parameters that fit the relative values of the 10-day dilutions, but their fit for the

original 20-day batch culture is not as close as the one obtained at the end of step 4, although still capturing the features of the original growth curves and, of course, the relative magnitude of the abundance values at time 10 vacillate. As explained above, this is a necessary and expected result as the highly variant 10 day dilution values cannot have inter-dilution growth curves identical to the original growth curves.

Examples of Calibrated Systems

Steps (1.-4.) of calibration methodology, the section Calibration Methodology, produce different results depending on the specific loss function used. Here we used two least square loss functions:

$$\sum_{i=1}^{n}\sum_{j=1}^{k} w_{ij}(x_i(t_j) - \hat{x}_i(t_j))^2 \quad \text{and} \quad \sum_{i=1}^{n}\sum_{j=1}^{k} w_{ij}(\log(x_i(t_j)) - \log(\hat{x}_i(t_j)))^2, \tag{S13}$$

a residual squared error and a residual squared error of the log-transformation respectively, either of which may be weighted. The log-transformed least-squares better captures the dynamics in the values closer to zero, while the standard least-squares, both with $w_{ij} = 1$ for all i, j, more closely approximates the dynamics of the larger values. Choosing different weights similarly produces slightly different results.

Figures **S5** and **S6** show the results of the calibration steps (1.-4.). Panels (A), (B), and (C) of figure **S5** show the result of calibrating with respect to the log-transformed data, which produced parameter set Π_1, see Table **S1**. The subsequent sets of three panels (D, E, F), and (H, I, J), and (K, L, M) of figure **S6** each correspond to the parameter sets Π_2, Π_3 and Π_4 of Table **S1**, respectively. The parameter set Π_2 was obtained with unweighted squared error. For parameter sets Π_3 and Π_4 the later data points were weighted more heavily. In particular parameter set Π_3 was obtained using standard least squares with a weight of 100 at the final time $t = 20$ and a weight of 1 for all other times. Parameter set Π_4 was obtained using a weighted residual of the log-transform of the data; specifically a weight of 10 for all values of t such that $t \geq 10$ and a weight of 1 for all $0 \leq t < 10$.

If we take the parameters found for panels (A), (B), and (C) of figure **S5** and evaluate the dilution map, defined in (3), out to 20 dilutions with 10 days between dilutions, we see in panels (A) and (B) of figure **S7** that the dilution map $Y(t)$ converges to a periodic solution which corresponds to a constant solution of the discrete map whose values are $Y(10n+)$. Indeed all of the parameter sets Π_1, Π_2, Π_3, and Π_4 that result from steps (1-4) of the section Calibration Methodology create dilution maps with similar long term behavior; that is, the discrete map converges quickly to a state where $X_1 > X_2$ and X_2 approaches 0.

The results of steps 5-7 of the section Calibration Methodology, are displayed in figure **S8**. We provide three examples of the system defined in definition 4 fitted to specific measurements of coculture serial dilution lines. In figure **S8** the left hand column plots the relative abundance values of $Y(10n+)$ for $n = 0, 1, 2, \ldots 9$ and the right hand column plots the absolute abundances on a log scale. Panels pairs (A, B), (C, D), and (E, F) correspond to parameters Π_5, Π_6, and Π_8 of table **S2** respectively. Note that all parameter sets Π_1 through Π_4 do not serve equally well for starting points steps (5-7). When we construct the box P over which we uniformly sample in step 5, the bounds we choose are proportional to the initial values p^* in the form $l_i' = ap_i^*$ and $u_i' = \max\{bp_i^*, \mu\}$. If we take a and b to be 0.5 and 2.0, random sampling provides very few parameters sets with nonconvergent or slowly converging discrete maps. Using Π_3 or Π_4 as starting

point, the larger interval around β_{11} allows for more variant discrete map orbits and following step 7 provides significantly closer fits to the 10 day dilution lines. While we do not closely recapitulate the absolute abundances, panels (A), (C), and (E) show a surprisingly close fit to the highly variant empirical relative abundances. We show in the following section that these parameters occur in sections of the parameter space where one finds chaotic behavior of the discrete map.

Transition to chaotic behavior

Chaotic orbits of Dynamical Systems arise when those systems are extremely sensitive to small changes in initial conditions. This sensitivity to initial conditions is measured by the *Lyapunov Exponent* (*4*). The Lyapunov exponent describes how a small set of initial conditions around a point x_0 converge or diverge from the orbit generated by x_0 through repeated iterations of a map. In our case we are interested in the Lyapunov exponent associated to the discrete map, definition 4, for a fixed set of parameters defining the underlying system and a fixed dilution time τ. Letting $\delta = \hat{x} - x_0$ be a small perturbation of the initial point x_0 and let DH_τ be the Jacobian of the discrete map H_τ. The Lyapunov exponent of the H_τ with respect to δ is defined as the limit

$$\lambda = \lim_{n\to\infty} \frac{1}{n} \log \| DH_\tau^{(n)}(x_0)\delta \| \tag{S14}$$

assuming it exists; where $H_\tau^{(n)}$ is the nth application of the map H_τ. In general to capture all dimensions of perturbation this is computed instead by taking a unit ball, B, around the point x_0 and evolving it forward, again, by the linearized dynamics as $DH_\tau^{(n)}(x_0)B$. If $r^{(n)}$ is the largest radius of the ellipsoid $DH_\tau^{(n)}(x_0)B$ then we define the Lyapunov exponent of H_τ at x_0 as

$$\lambda = \lim_{n\to\infty} \frac{1}{n} \log r^{(n)}. \tag{S15}$$

Computationally the matrix $JJ^\intercal$ for $J = DH_\tau$ can become extremely ill conditioned and thus various normalization methods have been introduced. We compute Lyapunov exponents with the `ChaosTools.jl` package (*5*) which uses the 'H2' method of (*6*) originally published by (*7*). For additional details see (*8*).

Many solutions to the serial passage system given in definition (3) have convergent solutions in sense that the values of $Y(n\tau)$ converge to a fixed point in $\mathbb{R}^n$ as $n \to \infty$, which corresponds to a periodic solution of the discontinuous semi-flow $Y(t)$ for $t > 0$. But as we have seen empirically, figure **S4**, these relationships do not display obviously convergent behavior. The relative abundances can be recapitulated as in figure **S8**, and these solutions exist in regions of the parameter space that display chaotic behavior.

Let us consider example 3 from figure **S8**, which has parameters Π_8 of table **S2**. The orbits of the discrete map do not display obviously convergent or periodic behavior. To test whether we observe chaotic behavior, we can calculate the Lyapunov exponent. For example 3 from figure **S8**, the Lyapunov exponent, calculated out to $100,000$ iterations, is approximately 0.117, indicating chaotic trajectory. The first dimension, X_1, is constant but X_2 and R_2 are highly variant resulting in the high Lyapunov exponent.

We can observe the transition to chaos for this example by interpolating between a set of parameters with convergent discrete map, Π_1 of table **S1**, and the parameters that fit the relative abundances

of example 3, Π_8. In figure **S9**(A) we simply perform a linear interpolation $(1-s)(\Pi_1)+s(\Pi_6)$ for $s \in [0,1]$ to produce a bifurcation diagram. Panel (A) of figure **S9** shows the orbits of X_2 for a particular value of s in the previously mentioned interpolation. In particular if $\{X_2^{(i)}\}_{i=0}^{\infty}$ is the sequence of X_2 values generated by the discrete map with respect to a particular parameter set, panel (A) plots the values $X_2^{(1001)}, \ldots, X_2^{(1100)}$. This creates a classical bifurcation diagram; initially X_2 values converge to zero, then undergo a period doubling bifurcation and then have chaotic orbits with isolated periodic regions which include period 3 orbits. Panel (B) plots the approximate Lyapunov exponents of the discrete map at each interpolation point. This shows, as one would expect, negative Lyapunov exponents for convergent and periodic regions and positive Lyapunov exponents in the chaotic regions. Example system 1 is very similar to example system 3, in the sense that the parameters Π_5 have positive Lyapunov exponent and the bifurcation diagram when interpolating between Π_1 and Π_5 is very similar to figure **S9**.

The particulars of the bifurcation diagram or the Lyapunov exponent are not the same for all examples. They differ in fact within a single example. The calibration procedure does not guarantee a unique minimum and can produce different results when starting from different initial conditions and choosing different sets in the parameter space. Figure **S11** contains several bifurcation diagrams related to example system 2 of figure **S8**. We provide separate calibrations of example system 2, one using initial parameters Π_3 (Table **S1**) and producing parameters Π_6 (Table **S2**), the result of which is shown in panels (A) and (B) of figure **S10**. The second calibration, using Π_4 (Table **S1**) as initial parameters and producing parameters Π_7 (Table **S2**), is plotted in panels (C) and (D) of figure **S10**. Two bifurcation diagrams presented in panels (A) and (C) of figure **S11** both have parameter set Π_7 as the final parameter set, but they interpolate from initial sets Π_1 and Π_3, respectively. We can see that, not surprisingly, taking different lines through the parameter space creates distinct bifurcation diagram though they end at the same point. Parameter set Π_6 similarly recapitulates example 2 but does not have positive Lyapunov exponent. The bifurcation diagram interpolating between Π_1 and Π_6 is given in panel (E) of figure **S11**, and it shows the existence of chaotic regions, although set Π_6 (the rightmost region of the bifurcation diagram) falls in an isolated region of periodic dynamics with period three. Thus the chaotic quality is not inherent when calibrating to specific culture lines, but these variant coculture values lie near chaotic regions of the parameter space.

The dilution time parameter, τ, also plays a crucial role in the behavior of the discrete map. Fixing the parameters to Π_8, and evaluating the orbits for values of τ between $\tau = 3$ and $\tau = 14$ days we see a transition to chaos with τ as the bifurcation parameter (figure **S12**), as we did in figure **S11**. So, not only do the interactions result in a bifurcation, but the frequency of dilution also determines the long term behavior of the orbits of the discrete map.

Chaos in the gLV model with resampling

So far we have demonstrated that a transition to chaotic behavior can be observed in a system where (1) two species are involved in asymmetric crossfeeding (that is, where one species requires the other in order to grow); where (2) growth equations are fully mediated by endogenous resource concentrations; and (3) a process of serial transfers takes place introducing discontinuities into the abundance and concentration trajectories. Note that the underlying gLV system in many cases converges in the absence of serial transfers.

It turns out that the transition to chaotic behavior can be observed in simpler models that describe

co-dynamics of two species in a resampled system. Consider a gLV model with resampling, which was studied in (*9*):

$$\begin{aligned} \dot{x}_1^{(j)} &= b_1 x_1^{(j)} + \textstyle\sum_{k=1}^{m} a_{1k} x_k^{(j)} x_1^{(j)} \\ &\vdots \\ \dot{x}_i^{(j)} &= b_i x_i^{(j)} + \textstyle\sum_{k=i}^{m} a_{ik} x_k^{(j)} x_i^{(j)} \\ &\vdots \\ \dot{x}_m^{(j)} &= b_m x_m^{(j)} + \textstyle\sum_{k=1}^{m} a_{mk} x_k^{(j)} x_m^{(j)} \end{aligned} \tag{S16}$$

where b_i and a_{ik} are constants for all i and k, m is the number of interacting subpopulations, and the superscript, j, numbers the "frame" (that is, the period of time between resamplings). The initial conditions for each of these systems are given by setting x_i to be proportional to the relative abundance of x_i at the terminal point of the previous frame,

$$x_i^{(j)}(t_{j-1}) = \nu \frac{x_i^{(j-1)}(t_{j-1})}{\sum_{k=1}^{m} x_k^{(j-1)}(t_{j-1})}, \tag{S17}$$

where ν is a constant that determines the volume of the transferred culture and $x^{(1)}(0) = x_0$ is given. Note that the system described by equations (S16) and (S17) corresponds to a serial transfer system where the underlying dynamics are given by the gLV equations and the instantaneous transfer function ϕ is given by $\phi_i(x) = x_i / \sum_j x_j$.

Taking the simplest case of $m = 2$, the sequence

$$(x_1^{(j)}(t_{j-1}), x_2^{(j)}(t_{j-1})), \quad j = 1, 2, \ldots$$

can be described by a 1D map, as, for the $m = 2$ case, we must have $x_2^{(j)}(t_{j-1}) = \nu - x_1^{(j)}(t_{j-1})$.

Definition 5. (gLV Resampling Map) Define the map $F_t : [0, \nu] \to [0, \nu]$ by

$$F_t(y) = [\phi \circ U(t, (y, \nu - y))]_1 \tag{S18}$$

where U is forward operator associated to the 2-dimensional gLV system

$$\begin{aligned} \dot{x}_1 &= b_1 x_1 + a_{11} x_1^2 + a_{12} x_1 x_2 \\ \dot{x}_2 &= b_2 x_2 + a_{21} x_2 x_1 + a_{22} x_2^2 \end{aligned} \tag{S19}$$

and ϕ is the proportional resampling instantaneous transfer function defined by

$$\phi((x_1, x_2)) = \frac{\nu}{x_1 + x_2}(x_1, x_2). \tag{S20}$$

That is, F_t takes a point $y \in [0, \nu]$, interprets it as the initial value of the first dimension of equation (S19), assigns $\nu - y$ as the initial value of the second dimension, evolves them forward according to (S19) to time t, then applies the resampling map, and returns the value of the first dimension. We refer to equation (S19) as the *gLV system*.

We consider sequences generated by a fixed resampling time $\tau \in (0, \infty)$. The set of points, $\{y_n\}_{n=0}^{\infty}$ defined by

$$y_{n+1} = F_\tau(y_n), \text{ for some } y_0 \in [0, \nu] \tag{S21}$$

we call an orbit of F_τ.

This is a convenient map to investigate with respect to its trajectories as it is one-dimensional. It is continuous and maps a closed interval to itself, so it must have a fixed point. Indeed, F_τ has at least two trivial fixed points, ν and 0. In reality, F_τ often exhibits fixed points on the interior.

Below we present three examples of gLV systems that are characterized by different types of behavior.

gLV System 1. Let us consider the system

$$\begin{aligned} \dot{x}_1 &= 0.1x_1 - 0.6x_1^2 + 0.4x_1x_2 \\ \dot{x}_2 &= 0.2x_2 + 0.2x_2x_1 - 0.5x_2^2 \end{aligned} \tag{S22}$$

with $\tau = 1$, $\nu = 1$, and let $y_0 = 0.5$. System (S22) has fixed points $(0, 0)$, $(0, 2/5)$, $(1/6, 0)$, and $(13/22, 7/11)$, where the strictly positive fixed point is asymptotically stable. Some properties of system (S22) are shown in panels (A), (B), and (C) of figure **S13**. We see the underlying gLV system converges to its only stable fixed point in panel (A), and panel (B) indicates the location of the interior fixed point of F_τ, the resampling map. The stable point of the underlying gLV system and the fixed point of F_τ do not correspond to the same values. The fixed point of F_τ depends on the value of τ and the speed of the underlying gLV dynamics. More specifically, if the gLV system converges to $(\hat{x}_1, \hat{x}_2)$ and F_τ is convergent, then the larger τ is the closer the fixed point of F_τ is to the value $\hat{x}_1/(\hat{x}_1 + \hat{x}_2)$.

We see from panel (B) of figure **S13** that not only does F_τ map $[0, 1]$ to itself, but if one takes a smaller interval containing the fixed point, say $[0.25, 0.75]$, then F_τ also maps this interval to itself, thus F_τ must converge to its internal fixed point. This can be seen clearly in the orbits of F_τ shown in figure **S14**.

gLV System 2. Next, we consider the following set of parameters for the gLV model:

$$\begin{aligned} \dot{x}_1 &= 0.3247x_1 - 0.0038x_1^2 + 1.1787x_1x_2 \\ \dot{x}_2 &= 4.9591x_2 - 0.0432x_2x_1 - 0.0541x_2^2 \end{aligned} \tag{S23}$$

with $\tau = 1$, $\nu = 1$, and $y_0 = 0.5$. Here we have the property that $a_{12}a_{21} < 0$. The only stable fixed point of equation (S23) is the nonzero point which is approximately (114.557, 0.096).

As before, the map has a single internal fixed point, call it $\hat{y}$, but in contrast to the previous example, we have $|D_y F_\tau(\hat{y})| > 1$. Note that $|D_y F_\tau(\hat{y})| > 1$ implies that F_τ cannot converge to this internal fixed point from an arbitrary initial value in $[0, 1]$. This scenario gives rise to chaotic orbits of the map F_τ with classical bifurcation phenomena. See figure **S14** panel (B) for the initial orbits of F_τ.

In figure **S15** we keep the parameters of the gLV system as they are given by equation (S23), except the parameters a_{12} and a_{21}, which we vary in a given interval. Panel (A) shows the bifurcation

diagram of F_t resulting from varying a_{21} and holding all other parameters constant. The approximate Lyapunov exponents appear below the corresponding orbit. In panel (B) of figure **S15** we vary a_{21} and hold all other parameters constant, and in panel (C) we vary a_{12} and a_{21} simultaneously and plot the sign the Lyapunov exponent, denoted as λ. The green points indicate $\lambda > 0$ and thus chaotic trajectories; the gray points indicate $\lambda < 0$.

gLV System 3. There are parameter sets, which have multiple internal fixed points, none of which the resampling map will converge to. Consider the system

$$\begin{aligned} \dot{x}_1 &= 0.4095x_1 + 0.0242x_1^2 - 0.407x_1x_2 \\ \dot{x}_2 &= -0.4367x_2 + 0.6013x_2x_1 - 0.0083x_2^2 \end{aligned} \tag{S24}$$

with constants $\tau = 24$, $\nu = 1$, and $y_0 = 0.5$. The fixed points of this system are approximately given by (0,0), (0, 52.5), (-16.9, 0), and (0.71, 1.048). The only stable fixed point is (-16.9, 0), but definitionally, initial values must be nonnegative. As (0,0) is an unstable fixed point, any initial values that start in the positive reals will stay positive but not converge to any of the positive fixed points. Note that the map, F_τ, has five internal fixed points, for all of which the derivative $|D_y F_\tau(y)| > 1$. This scenario too produces chaotic trajectories, see figure **S14**(C). In figure **S16** we plot a bifurcation diagram varying a_{11} and holding all other parameters constant.

Note that in each chaotic example the off diagonal interaction coefficients have opposite signs, that is $a_{12}a_{21} < 0$. We have not observed chaotic solutions for the resampling map when this inequality is reversed.

Figures

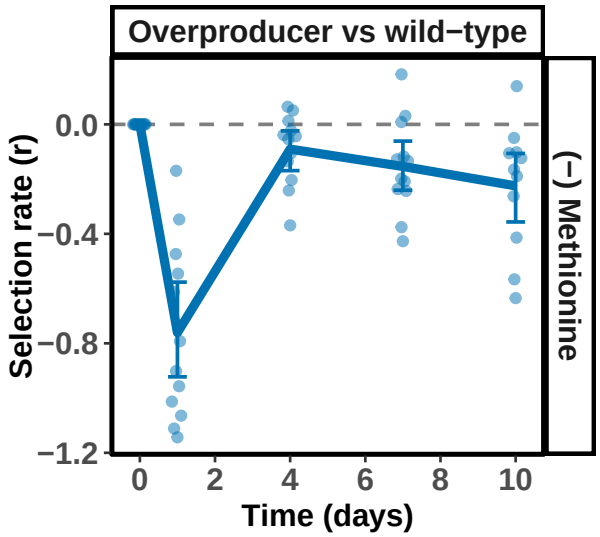

Fig. S1: **Overproducer fitness against wild-type *E. coli* K-12 in mM9 + 0.2% glucose.** The overproducer Δ*metJ E. coli* strain was co-cultured with wild-type K-12 for a continuous 10-day period (n = 12). Each strain was initiated from a single colony overnight in 2 mL of modified M9 minimal medium + 0.2% glucose grown for 18 hours. Cells were washed twice with fresh mM9. Into 10 mL of mM9 + 0.2% glucose, 100 µL of washed wild-type and 150 µL of washed mutant strain Δ*metJ* were aliquoted into each tube (the knockout strain has a higher perceived mortality rate, therefore starting cell amounts were adjusted to achieve a 1:1 starting ratio). Each culture was homogenized and 100 µL samples were taken from at days 0, 1, 4, 7, and 10. Samples were serial diluted and plated on tetrazolium agar to differentiate between strains, and overproducer selection rate was calculated from the differences in its growth relative to wild-type using the difference in their Malthusian parameters across each number of days (see methods). Error bars indicate +/- 95% confidence intervals.

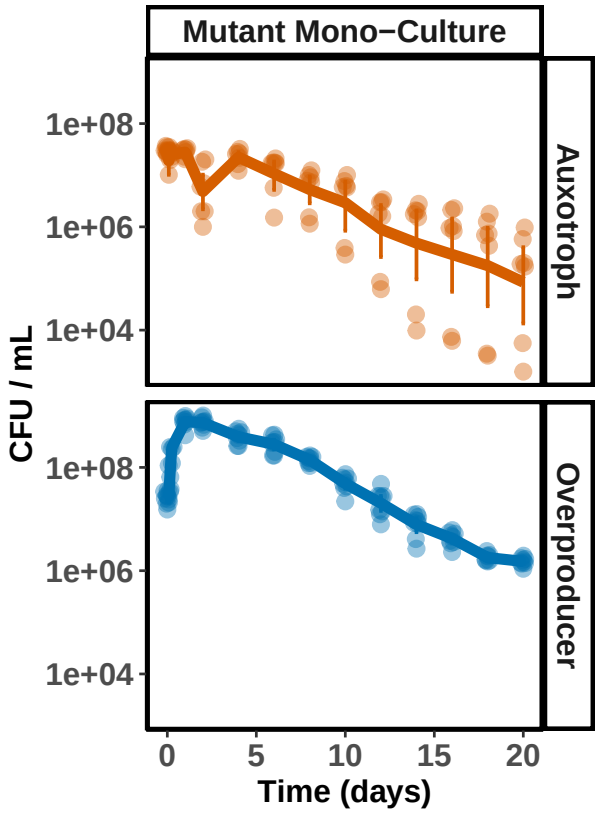

Fig. S2: **Death curves of the auxotroph and overproducer strains in monoculture conditions.** The overproducer Δ*metJ* and auxotroph Δ*metB* *E. coli* strains were cultured in isolation for a continuous 20-day period. Each strain was initiated from a single colony overnight in 2 mL of modified M9 minimal medium + 0.2% glucose grown for 18 hours. Cells were washed twice with fresh mM9. Into 10 mL of mM9 + 0.2% glucose, 100 µL of washed strains were aliquoted into each tube. Each culture (n =) was homogenized and 100 µL samples were taken every 2 days for 20 days. Additionally, the growth curve of each strain was manually collected by CFU plating every 2 hours until 12 hours of growth. Error bars indicate +/- 95% confidence intervals.

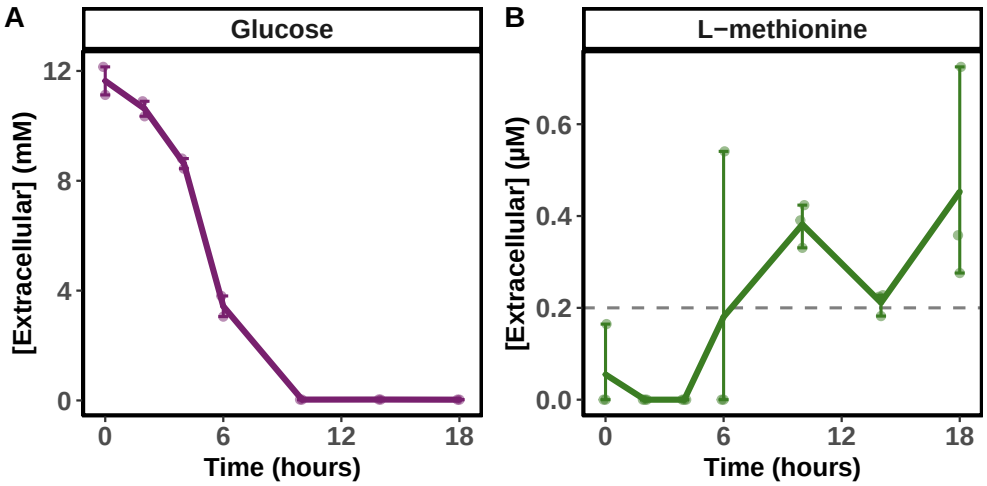

Fig. S3: **Measurements of extracellular glucose and L-methionine across an 18 hour period in overproducer Δ*metJ* monocultures.** (A) Glucose measurements in millimolar concentration across 18 hours (n=2). Samples were collected every 2 hours from 0 to 10 hours. Glucose became undetectable by 10 hours (assay measurements were collected and quantified at hours 14 and 18 and yielded no positive measurements). Error bars indicate +/- 95% confidence intervals. (B) L-methionine measurements in millimolar concentration across 18 hours (n=3). Samples were collected every 2 hours from 0 to 10 hours, and at hours 14 and 18. See Methods for collection and analysis methodology. Error bars indicate +/- 95% confidence intervals.

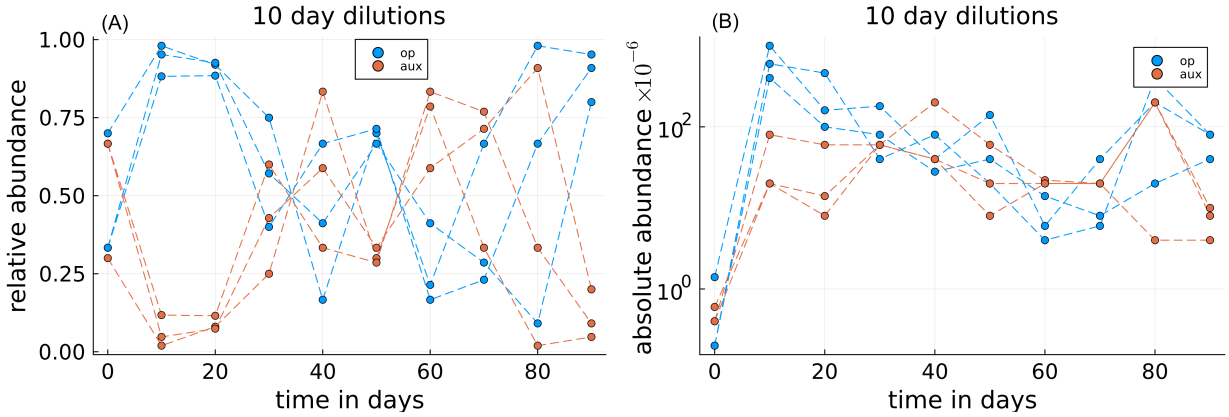

Fig. S4: **The empirical data for 3 serial dilution cultures.** The blue dots are measurements of the overproducer and the orange dots are the auxotroph. Panel (A) displays the relative abundance data and panel (B) displays the absolute abundance data. Note that the absolute abundance data, panel (B), is plotted on a log scale.

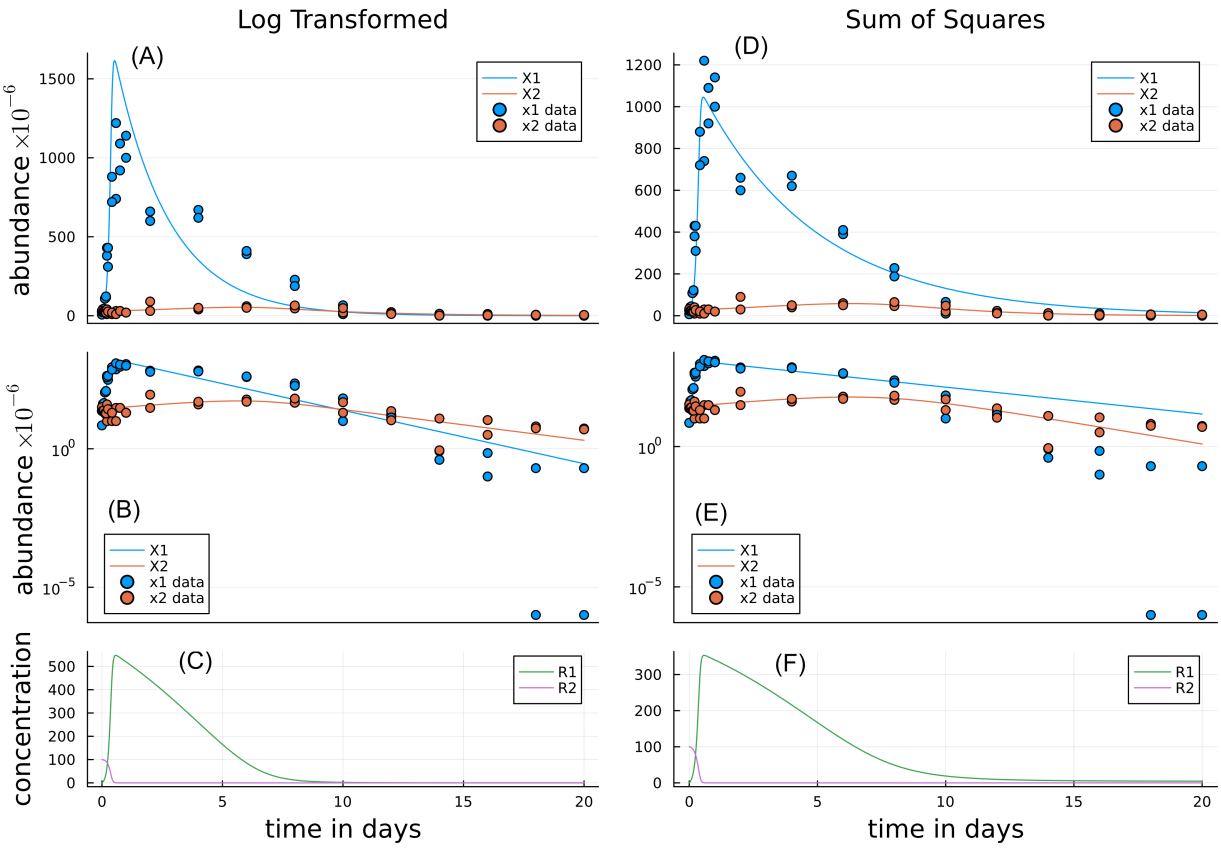

Fig. S5: **Initial calibrations, steps (1-4) of the section Calibration Methodology, of the model (S6) to a 20-day batch coculture with unweighted loss functions.** The left column, panels (A), (B), and (C), are fitted using the residual sum of squares of the log-transform of the data, thus weighting the smaller values heavily relative to the larger values and better capturing the behavior for absolute abundance near the minimal measurements. The right column, panels (E), (F), and (G), are calibrated using a standard residual sum of squares. This fits the larger values more closely but overestimates the smaller values. The parameters that produced (A), (B), and (C) are Π_1 of table **S1**, and the parameters that produced (D), (E), and (F), are Π_2.

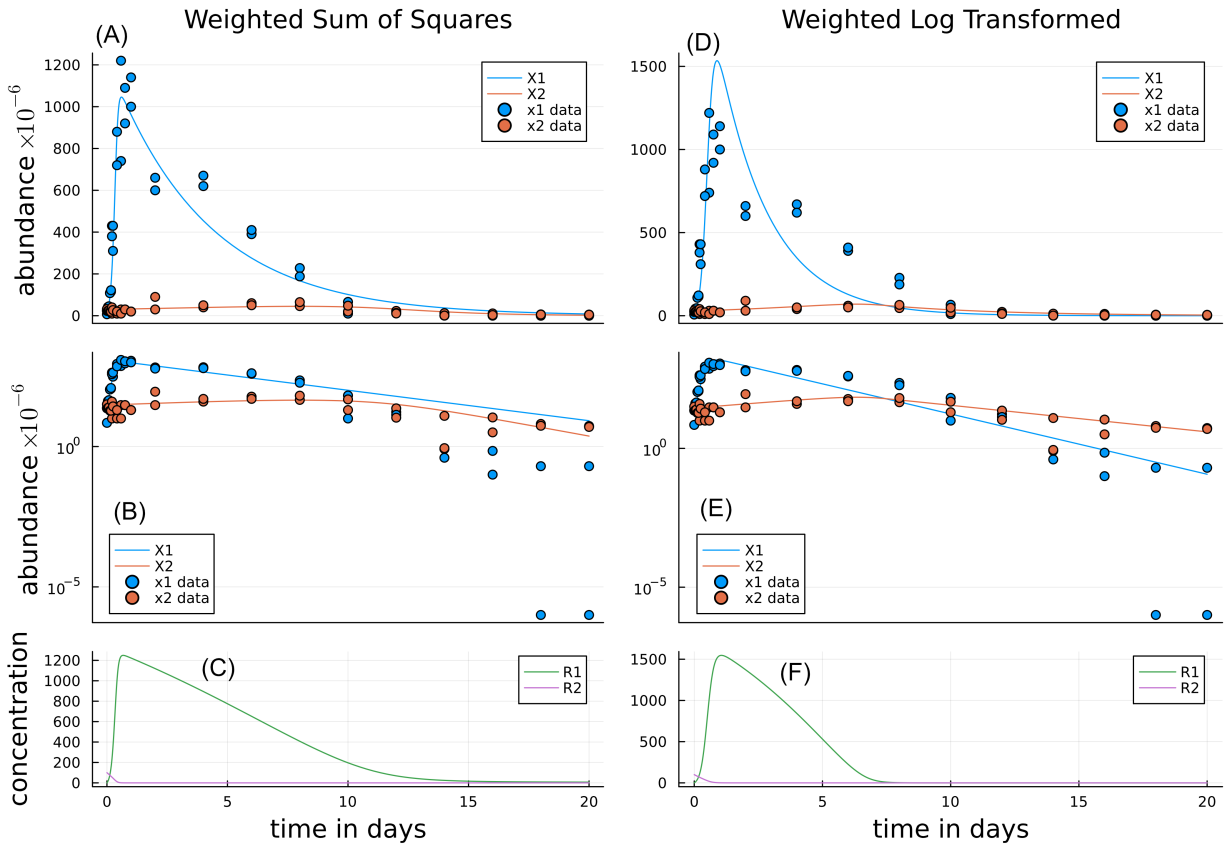

Fig. S6: **Initial calibrations, steps (1-4) of the section Calibration Methodology, of the model (S6) to a 20-day batch coculture with weighted loss functions.** Panels (A), (B), and (C), which correspond to parameters Π_3, were generated with a weighted least squares where the final time, $t = 20$, was given a weight of 100, for all data values and all other values were given a weight of 1. Panels (D), (E), and (F), which correspond to parameters Π_4, where generated with a weighted log-transformed residual, where all times t such that $t \geq 10$ were given a weight of 10 and given a weight of 1 otherwise.

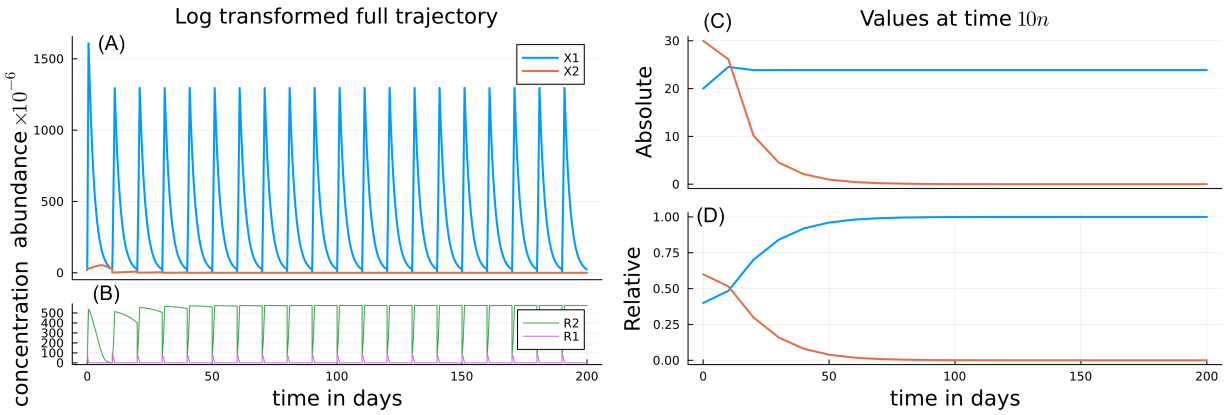

Fig. S7: **The trajectories of the dilution map, $Y(t)$, as defined in (3) for model (S6), with parameters Π_1 of table S1, fit to the underlying empirical data as shown in panels (C) and (D) of figure S5.** Panel (A) shows the trajectories of X_1 and X_2 and panel (B) shows the trajectories for R_1 and R_2 for $0 \leq t \leq 200$ thus representing the evolution of the system over 20 dilutions. Panel (C) is a line plot of only the values $X_i(10n-)$ for $n = 0, 1, 2, \ldots, 20$ and $i = 1, 2$, i.e. the absolute abundance values. Panel (D) is a line plot of the values $X_i(10n-)/\sum_{j=1}^{2} X_j(10n-)$ for $n = 1, 2, \ldots, 20$ and $i = 1, 2$, i.e. the relative abundance values. This is an example of a convergent system, in the sense that the discrete map converges to a constant value.

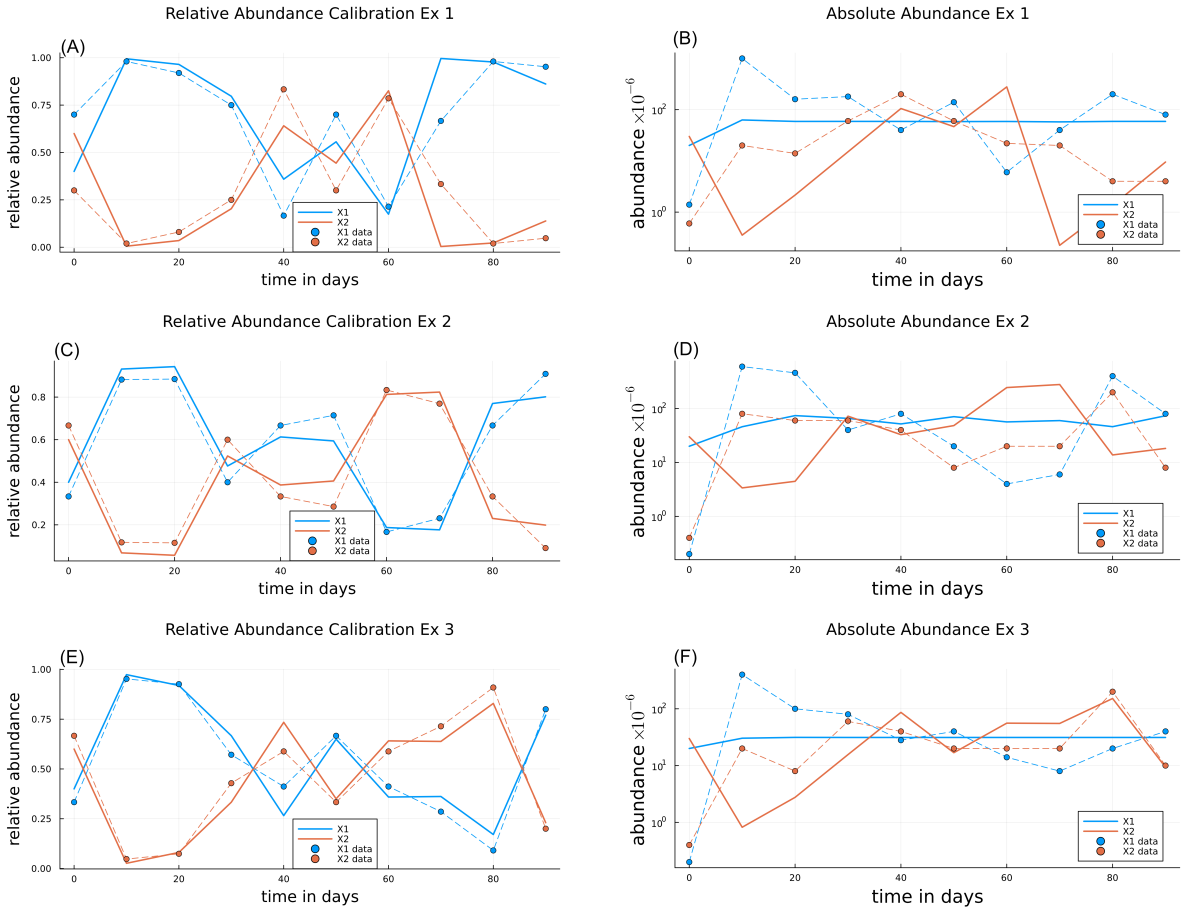

Fig. S8: **Plots of the three calibration examples.** The panel pairs (A, B), (C, D), and (E, F) each display the results of calibration to relative abundance values via steps (1-7) of the section Calibration Methodology. Dashed lines connect points which are CFU measurements of cultures. Solid lines denote values obtained from simulating a calibrated system. The left-hand side, panels (A), (C), and (E) display the relative abundance values and the right-hand side, panels (B), (D), and (F), display absolute abundance values on a log scale. The pairs (A,B), (C, D), and (E, F) correspond to parameters Π_5, Π_6, and Π_8 respectively.

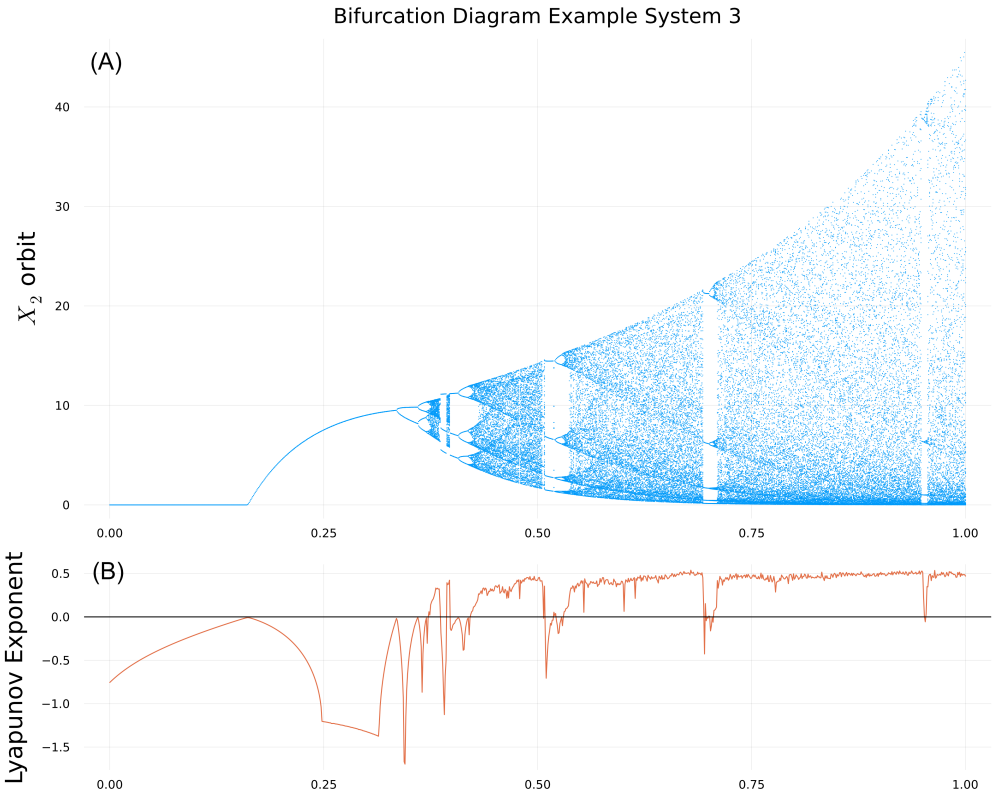

Fig. S9: **A bifurcation diagram of example system 3.** Panel (A) displays the orbits of X_2 and panel (B) is the Lyapunov exponent. We observe period doubling and the transition to chaos of the discrete map with intertemporal dynamics defined by model (S6). The x-axis denotes the value of s in an interpolation between parameter sets Π_{start} and Π_{end} of the form $\Pi_{start}(1-s)+\Pi_{end}s$ where $s \in [0,1]$. The parameters for panels (A) and (B) are $\Pi_{start} = \Pi_1$ and $\Pi_{end} = \Pi_5$. For panels (C) and (D) we have $\Pi_{start} = \Pi_1$ and $\Pi_{end} = \Pi_6$. The Lyapunov exponents, λ, satisfy $\lambda > 0$ for chaotic regions and $\lambda < 0$ for convergent and periodic regions.

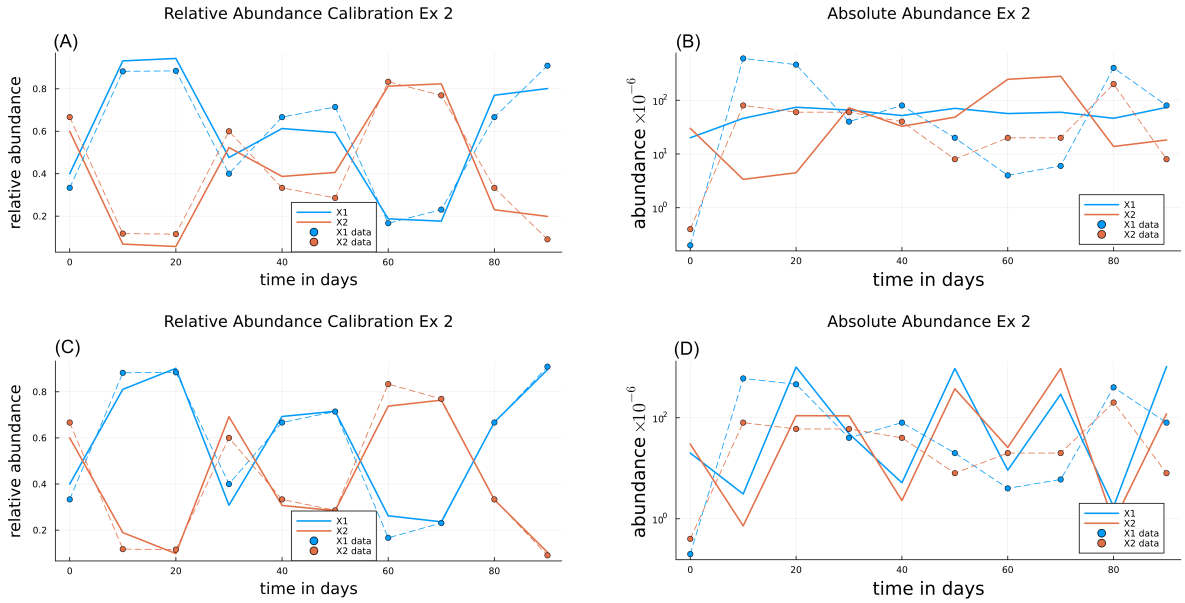

Fig. S10: **Different calibrations of example 2.** Panels (A, B) and (C, D) are distinct calibrations of Example 2 corresponding to parameters Π_6 and Π_7 (Table **S2**) respectively. The parameter sets Π_6 and Π_7 are the results of steps 5-7 of the section Calibration Methodology from initial points Π_3 and Π_4 (Table **S1**) respectively.

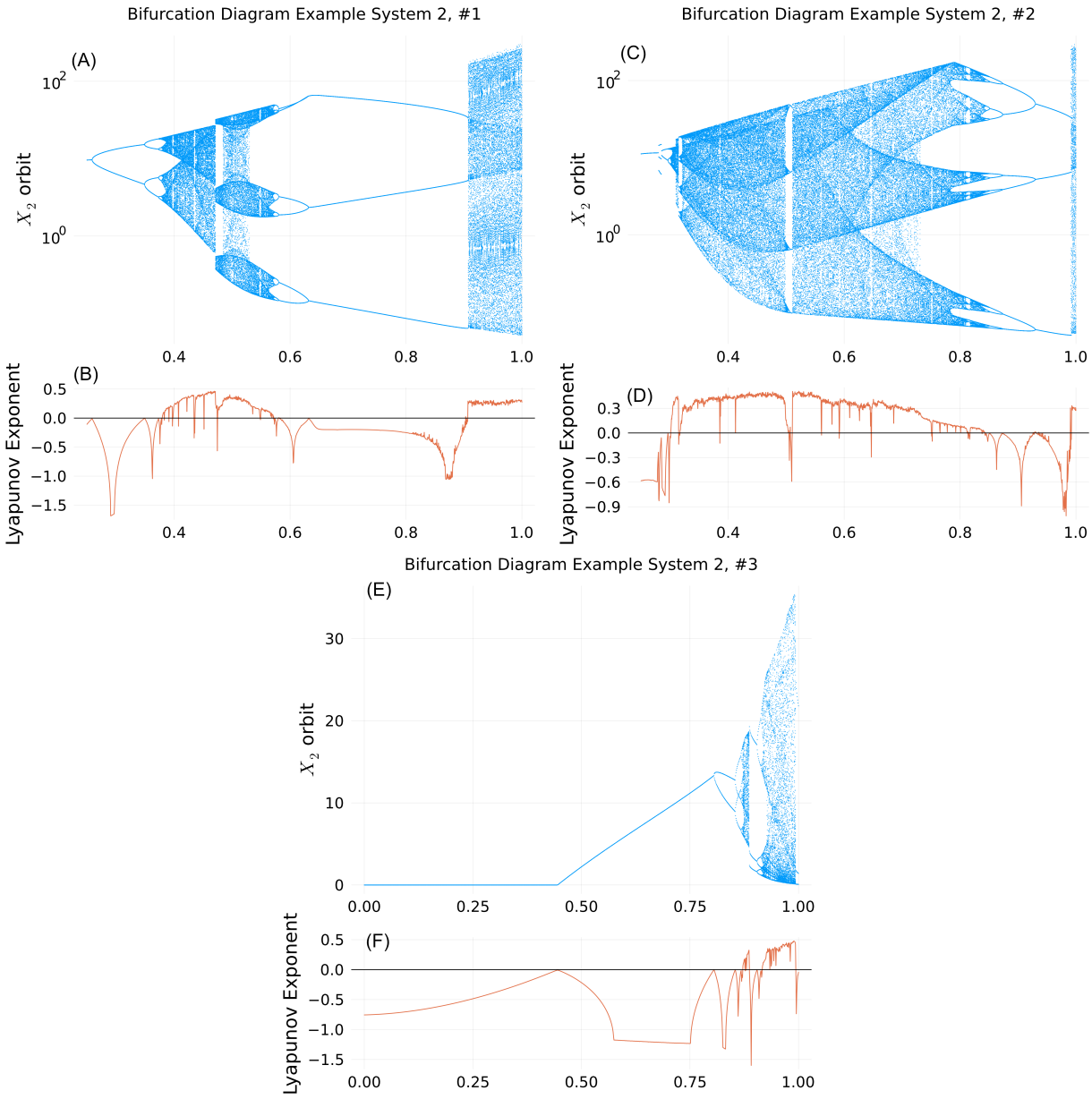

Fig. S11: **Bifurcation diagrams and Lyapunov exponent plots related to example 2.** Panels (A) and (B) are an interpolation between Π_1 and Π_7, (C) and (D) are an interpolation between Π_3 and Π_7, and (E) and (F) are an interpolation between Π_1 and Π_6. Panels (A) and (C) are both in log scale for better legibility. Note that Π_7, $s = 1$ for panels (A) and (C) is chaotic, and Π_6 which is the $s = 1$ orbit for panel (E) converges to a 3-cycle.

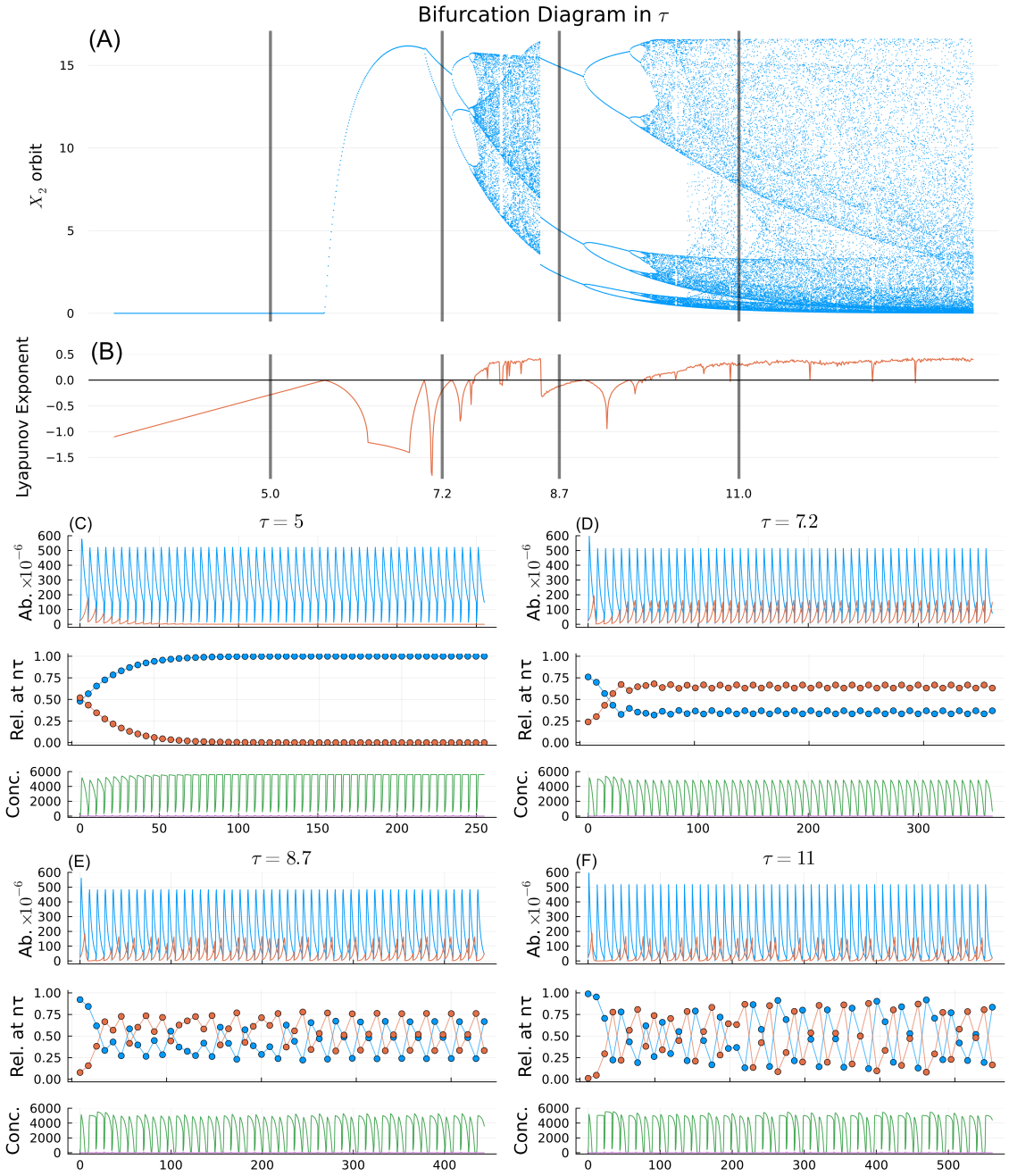

Fig. S12: **Plots describing the transition to chaos of example 2 where the bifurcation parameter is sample frequency.** Transition to chaos with τ (time between transfers) as the bifurcation parameter. Parameter set, Π_6 of table **S2** is used. (A) The bifurcation diagram with τ as the x-axis; shown is the orbit of X_2 of the discrete map for values of $\tau \in [3, 14]$. (B) The Lyapunov exponents over the same values. Panels (C), (D), (E), and (F) are plots of the dilution map $Y(t)$ and the associated discrete map over the course of 50 dilutions with τ days dilution frequency. For each of the panels (C), (D), (E), and (F) the sub-panels from top to bottom are the dilution map values of $X_1(t)$ and $X_2(t)$ in blue and orange lines, the relative abundance of the discrete map values of $X_1(\tau n)$, $X_2(\tau n)$ in blue and orange dots, and the dilution map values of $R_1(t)$ and $R_2(t)$ in green and purple lines.

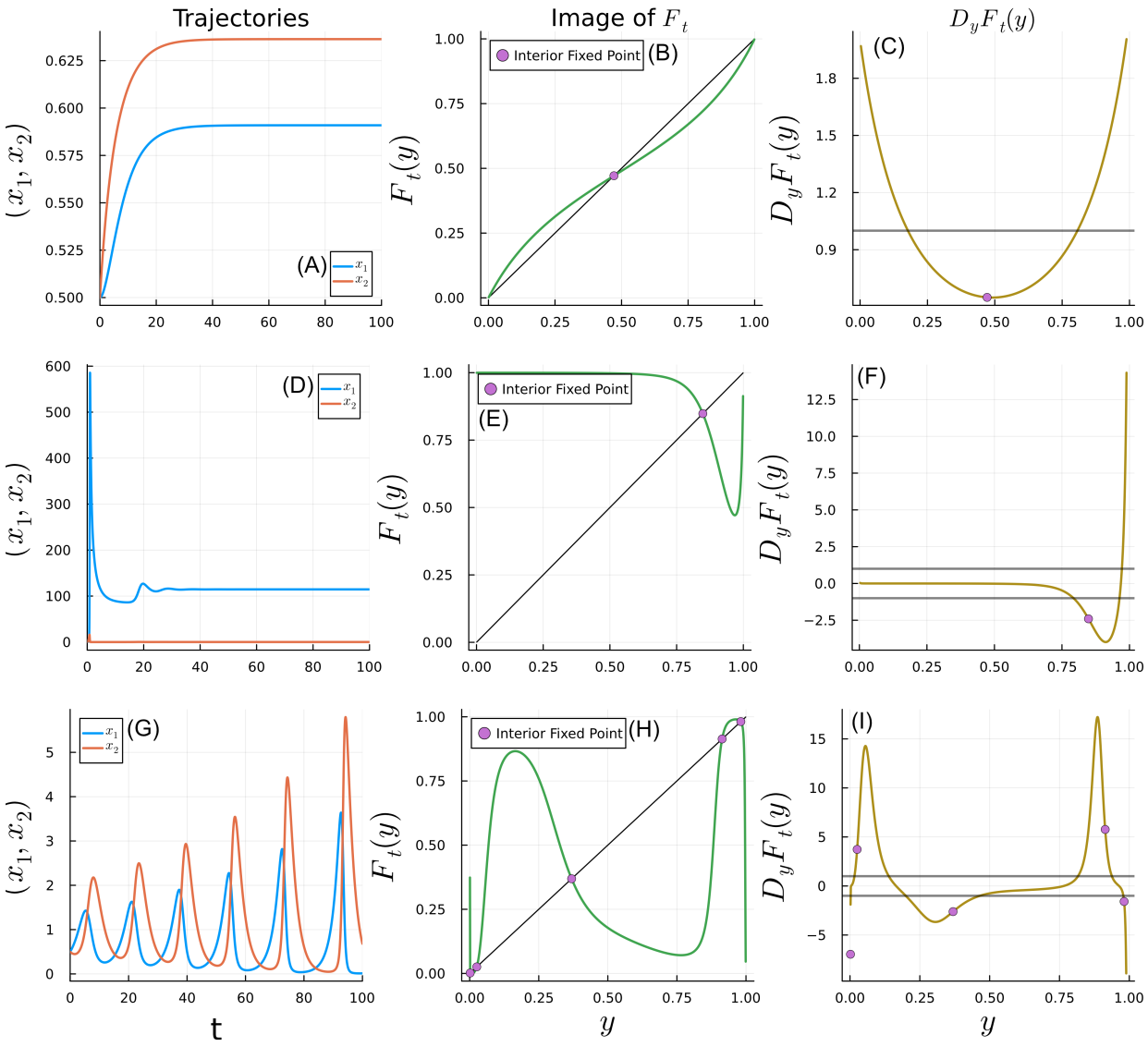

Fig. S13: **The qualitative behavior of the gLV system and the resampling map.** The top row, (panels (A-C)) correspond to Example system (S22), the middle row, (D-F), correspond to example system (S23) and the bottom row, (G-I), correspond to example system (S24). The left column, (A), (D), and (G), are the trajectories of the respective underlying gLV system. The center column, (B), (E), and (H), are the images of the respective resampling map, F_t, and the right most column shows the derivative of the resampling map. The internal fixed points are denoted as purple dots.

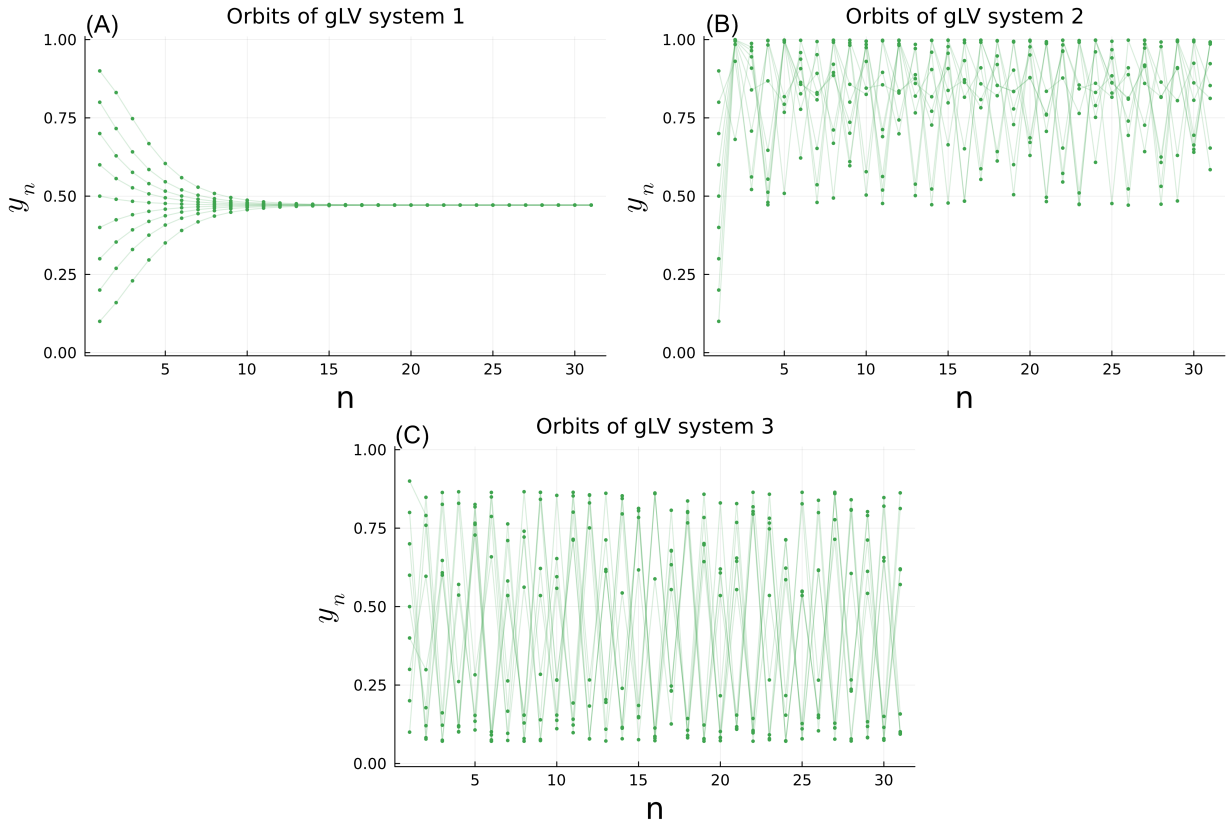

Fig. S14: **The initial orbits of the resampling map, F_t, for systems (S22), (S23), and (S24) from left to right.** Each panel contains 30 iterations of F_t starting from 9 initial points, $0.1, 0.2, \ldots, 0.9$. That is, they plot the sets $\{y_0, y_1, \ldots, y_{30}\}$ where $y_{n+1} = F_t(y_n)$ with $y_0 = 0.1, 0.2, \ldots, 0.9$. Panel (A) corresponds to the initial orbits of the resampling map of gLV system 1 where we clearly see the convergence of the resampling map to its fixed point. Panel (B) and (C) show the chaotic orbits of gLV systems 2 and 3 respectively.

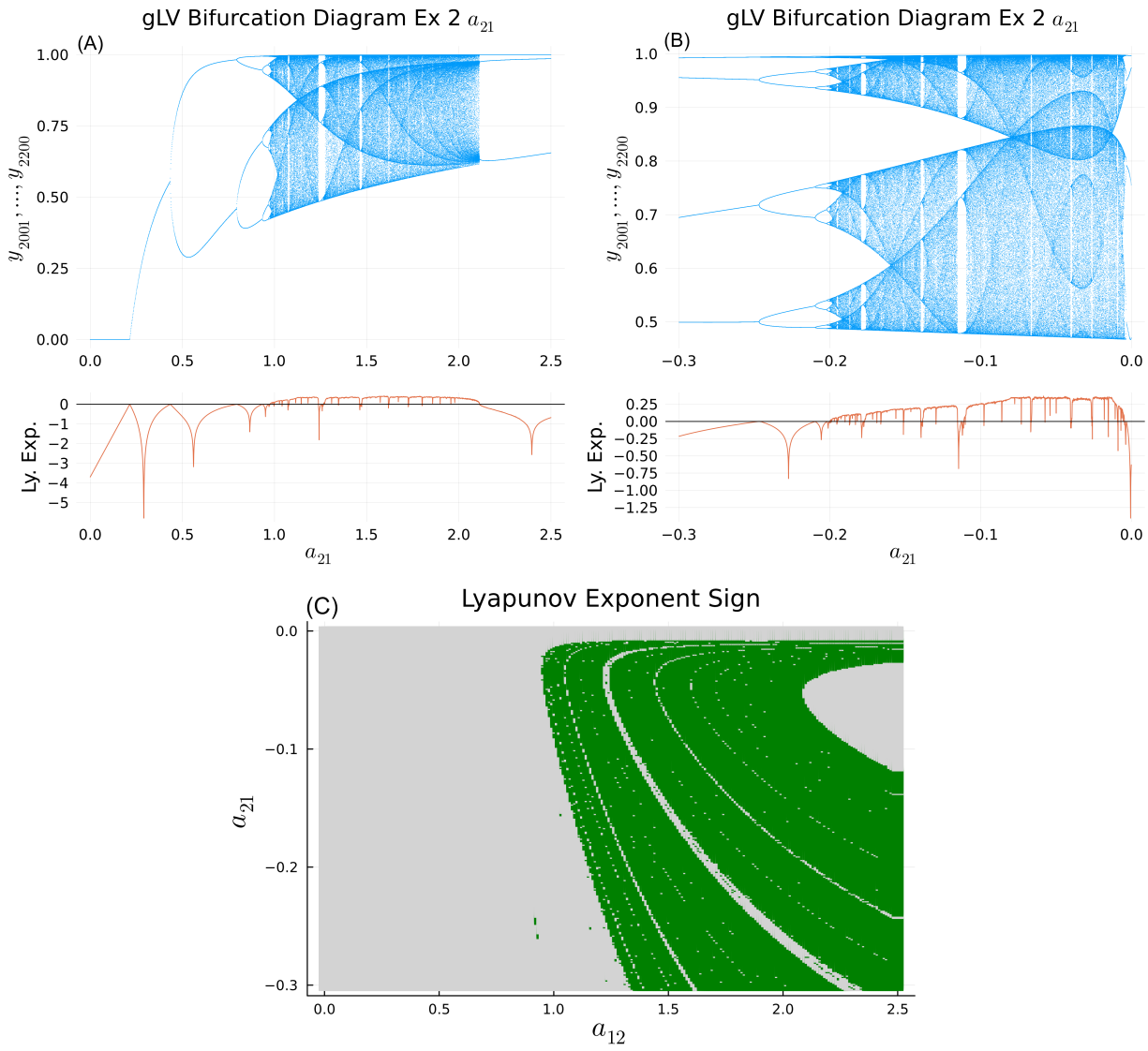

Fig. S15: **Bifurcations of the resampling map with gLV system 1, equations (S23).** Panel (A) contains the orbits of F_t on the top and the Lyapunov exponent on the bottom, as parameter a_{12} changes from 0.25 to 2.5. Panel (B) similarly contains the orbits on top and Lyapunov exponent on the bottom, for parameter a_{21} from -0.3 to 0.0. Specifically the portion of the orbits of F_t displayed are the 200 points from iterations 2001 to 2200. The bottom panel, (C), shows the sign of the Lyapunov exponent, λ, with gray indicating $\lambda < 0$ and green indicating $\lambda > 0$. In this panel both a_{12} (horizontal axis) and a_{21} (vertical axis) are varied.

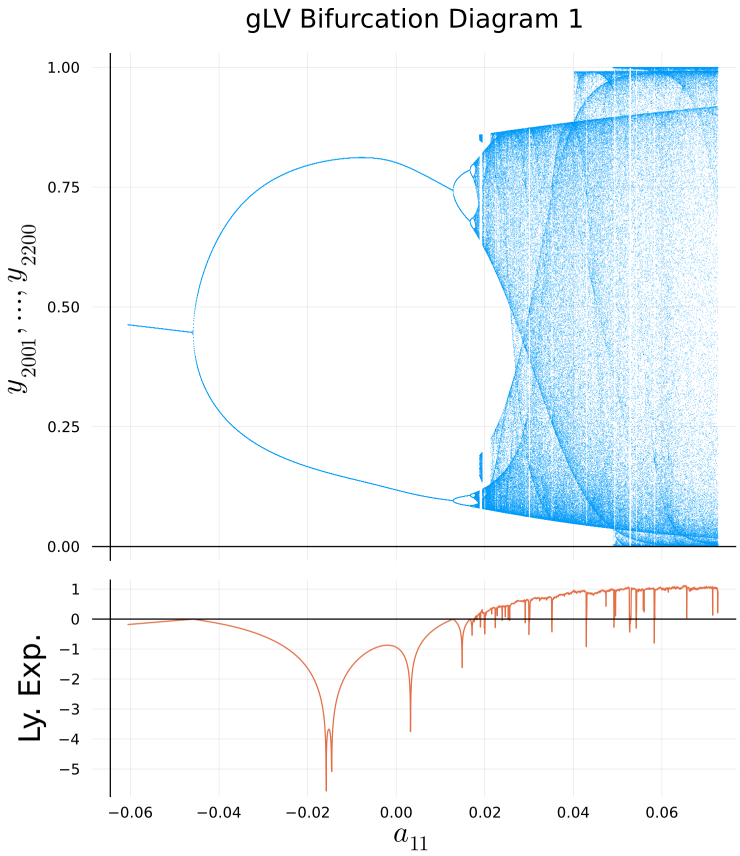

Fig. S16: **This figure contains the bifurcation diagram for the resampling map corresponding to equation (S24) in which we vary a_{11}.**

Tables

	Π_1	Π_2	Π_3	Π_4
b_{11}	021.576289641760773	17.647004280307897	023.2750389530667 83	028.030945506538735
b_{21}	000.4946654691247 0866	00.7151984174443384	000.5059225471404939	000.4236178598562 0026
b_{22}	000.0044488017808 18573	00.0044488027068634185	000.3499999999727 1225	000.1750000014360 0514
k_{11}	074.99999938163 03	62.322532229829 7	074.99999999871 63	149.99999873100478
k_{21}	097.52877100978 61	92.439424378532 32	121.58594177518263	128.39319843604 33
k_{22}	148.49902957352418	49.499726984899354	050.000000003766 8	099.99999985842923
d_1	000.4437450186381 8333	00.2206517417825 8318	000.2498768129475 6886	000.4997536258760 9146
d_2	000.2579156438584344	00.3850047494554 9484	000.3895826377760444	000.2203719385585063
β_{11}	006.991543173649346	05.923338681634315	027.0857622346681 3	024.8099728743873 38
β_{12}	002.713209008462893	01.365890724535 1297	003.4045172870051 49	006.2806335299178 86
β_{21}	001.216389120250 12	01.618446171980 7959	000.6868378558755645	000.3434189279390 5887
β_{22}	000.0209028853526 29987	00.0209029429993 67922	010.0811252408385 7	010.9369362135 4907

Table S1: **Parameter combinations that result from steps (1-4) of the section Calibration Methodology.** Loss functions used are unweighted log-transform, unweighted least squares, least squares with a weight of 100 at $t = 20$ and 1 elsewhere, and weighted log-transform with a weight of 10 for $t \geq 10$ and 1 elsewhere which correspond to Π_1, Π_2, Π_3, and Π_4 respectively.

	Π_5	Π_6	Π_7	Π_8
b_{11}	038.718638405405 05	002.106976622230 4986	023.931998870807 69	04.889020048624366,
b_{21}	002.686875124309263	003.071832943915211	001.288804669757824 6	01.650906058303704,
b_{22}	000.499539815329166 7	000.308362761913007 54	000.113228064762304 24	01.130458989828 2e-11,
k_{11}	036.746184946239 55	014.429657784664181	188.924683749662 88	18.254673464768086,
k_{21}	046.465098041255 19	148.799415341003 08	045.204754408018786	69.721395554294 86,
k_{22}	088.442656721509 51	009.901316969356856	087.467359458507 76	33.234926977846 05,
d_1	000.519755854415877 6	000.334548478390173 2	000.319263678973088 94	00.335411055983226 07,
d_2	002.264054138551831 6	002.484684372017271 3	000.478125356619547 25	01.212453405280162 8,
β_{11}	119.81773336194 79	014.748267523265 42	028.533750027233 19	41.099107055346 6,
β_{12}	028.335015307761 03	005.784561422268 1565	002.679753870132 352	12.420788537544 192,
β_{21}	000.371520972263 25376	000.235980317463 48647	000.135541372219 3278	00.733900056951 1533,
β_{22}	000.499768850928 141	000.499868216638 15784	034.478577367827 654	04.319009014851 37e-9

Table S2: **Parameters that correspond the example dilution lines presented in figure S8.** Parameters Π_5 produce example 1 of figure **S8**, Π_6 and Π_7 both correspond to example 2 and are presented in figure **S10**, and Π_8 produces example 3 of figure **S8**.

Movie S1. Generic example of ecotype co-dynamics across 25 dilutions under increasing dilution intervals. Ecotype dynamics between the overproducer (blue, X_1) and auxotroph (orange, X_2) across 25 dilutions as the dilution interval increases from 1 to 25 days. Top row indicates the absolute abundance of each competitor. Second from top indicates the abundance of each competitor at the time of dilution. Second from bottom indicates the relative frequency of each competitor at the time of dilution. Bottom row indicates the concentrations of resources 1 (primary carbon source) and 2 (secondary carbon sources) across a dilution period.

References and Notes

1. C. S. Holling, The Functional Response of Predators to Prey Density and Its Role in Mimicry and Population Regulation. *Memoirs of the Entomological Society of Canada* **97** (S45), 5–60 (1965), doi:10.4039/entm9745fv.

2. J. Monod, The Growth of Bacterial Cultures. *Annual Review of Microbiology* **3**, 371–349 (1949).

3. V. K. Dixit, C. Rackauckas, Optimization.Jl: A Unified Optimization Package, Zenodo (2023), doi:10.5281/ZENODO.7738525.

4. S. H. Strogatz, *Nonlinear Dynamics and Chaos: With Applications to Physics, Biology, Chemistry, and Engineering*, Studies in Nonlinearity (Addison-Wesley Pub, Reading, Mass) (1994).

5. G. Datseris, DynamicalSystems.Jl: A Julia Software Library for Chaos and Nonlinear Dynamics. *Journal of Open Source Software* **3** (23), 598 (2018), doi:10.21105/joss.00598.

6. K. Geist, U. Parlitz, W. Lauterborn, Comparison of Different Methods for Computing Lyapunov Exponents. *Progress of Theoretical Physics* **83** (5), 875–893 (1990), doi:10.1143/PTP.83.875.

7. G. Benettin, L. Galgani, A. Giorgilli, J.-M. Strelcyn, Lyapunov Characteristic Exponents for Smooth Dynamical Systems and for Hamiltonian Systems; a Method for Computing All of Them. Part 1: Theory. *Meccanica* **15** (1), 9–20 (1980), doi:10.1007/BF02128236.

8. G. Datseris, U. Parlitz, *Nonlinear Dynamics: A Concise Introduction Interlaced with Code*, Undergraduate Lecture Notes in Physics (Springer International Publishing, Cham) (2022), doi:10.1007/978-3-030-91032-7.

9. T. Beardsley, M. Behringer, N. L. Komarova, Detecting (the Absence of) Species Interactions in Microbial Ecological Systems. *Studies in Applied Mathematics* **154** (2), e70009 (2025), doi:10.1111/sapm.70009.